



HAL
open science

Tribological characterization of silicon carbide and carbon materials

Stéphanie Lafon-Placette, Karl Delbé, Jean Denape, Marc Ferrato

► **To cite this version:**

Stéphanie Lafon-Placette, Karl Delbé, Jean Denape, Marc Ferrato. Tribological characterization of silicon carbide and carbon materials. *Journal of the European Ceramic Society*, 2014, vol. 35 (n° 4), pp. 1147-1159. 10.1016/j.jeurceramsoc.2014.10.038 . hal-01154263

HAL Id: hal-01154263

<https://hal.science/hal-01154263>

Submitted on 22 May 2015

HAL is a multi-disciplinary open access archive for the deposit and dissemination of scientific research documents, whether they are published or not. The documents may come from teaching and research institutions in France or abroad, or from public or private research centers.

L'archive ouverte pluridisciplinaire **HAL**, est destinée au dépôt et à la diffusion de documents scientifiques de niveau recherche, publiés ou non, émanant des établissements d'enseignement et de recherche français ou étrangers, des laboratoires publics ou privés.



Open Archive Toulouse Archive Ouverte (OATAO)

OATAO is an open access repository that collects the work of Toulouse researchers and makes it freely available over the web where possible.

This is an author-deposited version published in: <http://oatao.univ-toulouse.fr/>
Eprints ID: 13692

Identification number: DOI: 10.1016/j.jeurceramsoc.2014.10.038
Official URL: <http://dx.doi.org/10.1016/j.jeurceramsoc.2014.10.038>

To cite this version:

Lafon-Placette, Stéphanie and Delbé, Karl and Denape, Jean and Ferrato, Marc
Tribological characterization of silicon carbide and carbon materials. (2014)
Journal of the European Ceramic Society, vol. 35 (n° 4). pp. 1147-1159. ISSN
0955-2219

Any correspondence concerning this service should be sent to the repository administrator:
staff-oatao@inp-toulouse.fr

Tribological characterization of silicon carbide and carbon materials

S. Lafon-Placette^a, K. Delbé^{a,*}, J. Denape^a, M. Ferrato^b

^a *Université de Toulouse, ENIT, LGP (Laboratoire Génie de Production), 47 Avenue d'Azereix, B.P. 1629, 65016 Tarbes, France*

^b *BOOSTEC, Zone Industrielle, 65460 Bazet, France*

Abstract

Tribological properties of a silicon carbide in homogeneous contact configuration are often related in lubricated or even dry conditions but only for ball or pin-on-disk configurations. The present study develops an experiment using a ring-on-ring device under dry friction in order to better match the industrial needs for dry mechanical seals applications. Tribological tests were run at a temperature of 120 °C, a sliding speed of 2 m/s and a contact pressure of 0.15 MPa on SiC/SiC and SiC/C pairs, with different impregnated carbon materials. The measurements were sensitive to the formation and the circulation of the third body at the contact interface. This third body was mainly composed by carbon, oxygen and the carbon impregnants. An amorphization process of the tribofilm was revealed by using Raman spectroscopy. Based on chemical analysis and mechanical considerations, the wear mechanisms were found to be driven by cracking process and oxidation.

Keywords: Silicon carbide; Carbon; Friction; Wear mechanism; Raman spectroscopy

1. Introduction

The development of new high-performance mechanical seals working in severe conditions requires higher material performances. Sintered silicon carbide (SiC), widely used as a hard mating material, is a potential candidate but its friction and wear properties need to be investigated in the scope of these new applications. Silicon carbide offers good mechanical properties (high hardness, high Young modulus), good corrosion resistance and good thermal conductivity, that make it suitable for tribological applications in different atmosphere (in air, argon or vacuum)^{1,2} and in dry or lubricated sliding.^{3,4} Overall, it shows a coefficient of friction in the range of 0.2–0.7 and a low wear rate, particularly when lubricated.^{5–7}

Combined with a counter-face ring made of a softer carbon–graphite, the dry sliding of SiC can be sustained even under severe conditions of pressure and speed.⁸ Graphite has been intensively studied in tribology since Bragg first described its lamellar structure. It has been thought during many years that

graphite could act as a solid lubricant because of this structure. In fact, the environmental conditions, as humidity, strongly influence its tribological behavior.^{9,10} The hardness of the ceramic facing the carbon seal has also an impact on its friction properties. A transfer layer of carbon is generally found on the ceramic surface.¹¹

This study deals with the tribological behavior of SiC sliding against SiC and two different carbon graphite materials in ring-on-ring configuration under dry friction.

2. Materials and methods

2.1. Material

As sample material for the primary ring, pressureless-sintered silicon carbide, SiC BOOSTEC[®], was used. It has a high homogeneous and fine microstructure, and it shows a closed porosity of less than 3.5 vol.% with a non-interconnected structure. The surface was polished to provide an arithmetic roughness Ra of less than 0.1 μm. Fig. 1 shows a scanning electron micrograph of the microstructure of this SiC etched by boiling Murakami's reagent (45 g of K₃Fe(CN)₆, 40 g of NaOH and 200 mL of H₂O). The average size of the silicon carbide grains is about 5 μm.

* Corresponding author. Tel.: +33 562442724; fax: +33 5624427208.
E-mail address: karl.delbe@enit.fr (K. Delbé).

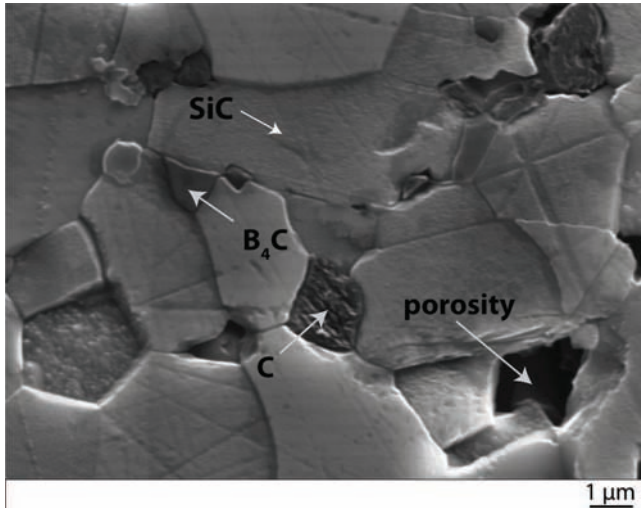


Fig. 1. Microstructure of SiC BOOSTEC® etched by Murakami's reagent.

Black regions are identified as graphite, boron carbide B_4C and porosities.

Two different carbon–graphite materials from MERSEN (Gennevilliers, France) were manufactured for counter-face rings: a polyester resin impregnated carbon–graphite (referred as $C_{(PES)}$) and an antimony impregnated carbon–graphite (referred as $C_{(Sb)}$). Impregnations are used to fill the porosities and shape the properties of the initial material. Polyester resin and antimony strengthens the carbon–graphite giving flexural strengths of 92 MPa and 128 MPa, respectively. Moreover, antimony, as a ductile metal, is considered as a solid lubricant by its ability to easily deform and to allow the accommodation at the interface. In the same way as for the SiC, the surfaces were polished to get $R_a < 0.1 \mu m$. Properties of the materials used in this work are summarized in Table 1.

2.2. Tribometer

Experiments were performed under dry friction using a ring-on-ring tribometer^{12,13} (Fig. 2).

This tribometer rotates the mating ring against the counter-face ring. The carbon ring dimensions were 38 mm outer diameter, 30 mm inner diameter and 13.5 mm height. For the SiC, it was 40 mm outer diameter and 30 mm inner diameter. The load is applied by means of dead weights. A torque and force sensor records continuously the applied normal force F_N

Table 1
Main properties of studied materials.

Material	Density (kg/m ³)	Hardness	Flexural strength (MPa)
$C_{(PES)}$	1800	110 Shore A	91.8
$C_{(Sb)}$	2330	107 Shore A	128
SiC BOOSTEC®	3180	2200 HV	450

and the resistant torque C_r . These parameters give the friction coefficient μ through Eq. (1):

$$\mu = \frac{3}{2} \times \frac{C_r}{F_N} \times \frac{r_1^2 - r_2^2}{r_1^3 - r_2^3} \quad (1)$$

where r_1 and r_2 are the outer and inner radii of the samples.

Tribological tests were run at 120 °C in ambient air. The sliding speed was 2 m/s and the contact force 64N giving a contact pressure of 0.15 MPa to a contact area of 428.5 mm². Experiments were conducted for two hours (total sliding distance of 14,400 m) inside a tighten enclosure. Three pairs of materials were tested: a SiC/SiC couple and two SiC/C pairs using the two supplied carbons $C_{(PES)}$ and $C_{(Sb)}$.

2.3. Characterization methods

Wear loss was measured by weighting the samples using a scale (R1809, Sartorius Research) with a degree of accuracy of ± 0.01 mg.

The topography and surface profiles of the worn ring specimens were determined using a 3D optical profilometer (Wyko NT1100, Veeco) and the surfaces of tested samples were all examined by optical microscopy as well as scanning electron microscopy (SEM-FEG 7000F, Jeol).

In association with SEM imaging, elemental chemistry of the wear tracks was analyzed by Energy Dispersive X-ray Spectroscopy (XFlash 4010, Bruker) using the same settings (accelerating voltage: 15 kV; working distance: 10 mm).

Raman micro-spectroscopy using a Horiba LabRAM HR 800 Raman confocal spectrometer with a confocal hole of 100 μm and the monochromator is a 1800 lines/mm holographic grating and an argon laser emitting at 532 nm provided chemical and structural characterizations of the samples. Using a 100 magnifying lens with a numerical aperture of 0.9, the spot diameter was 721 nm and the axial resolution was 2.6 μm .

3. Results

3.1. Friction coefficients

Fig. 3 presents the friction coefficients μ for each test as a function of sliding time or distance. At the beginning of the SiC sliding against SiC test (Fig. 3a), the friction coefficient was high and kept oscillating between 0.4 and 0.8. Then, at 2000 s it stabilized at a value of 0.15. The friction behavior of the SiC/ $C_{(PES)}$ pair was very different (Fig. 3b): the transitory period was reduced and the level of the friction coefficient was smaller with a mean value of 0.1 and showing short jumps up to 0.4 all along the test. Finally, for the last couple SiC/ $C_{(Sb)}$, high instabilities of the friction coefficient were observed all along the test without stabilization period (Fig. 3c). The coefficient of friction is also represented as box plots for the 3 studied compounds (Fig. 3d). This statistical representation confirms that the coefficient of friction of the SiC/ $C_{(PES)}$ couple is the lowest and the more stable of the study. The coefficient of friction of the SiC/ $C_{(Sb)}$ couple, the most disturbed.

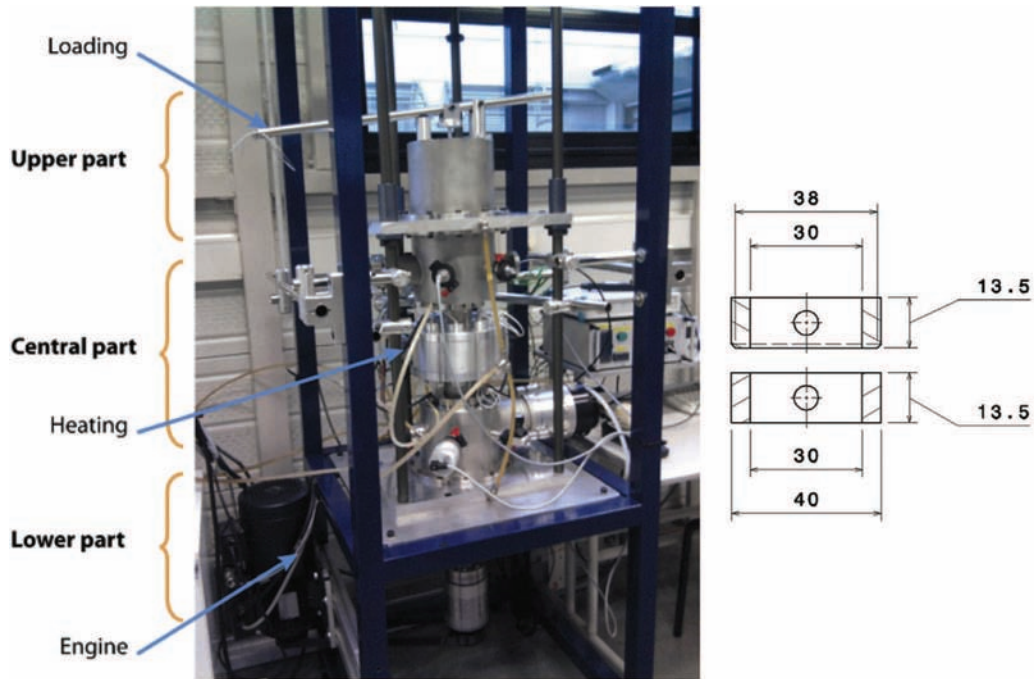


Fig. 2. Ring-on-ring tribometer and samples dimensions.

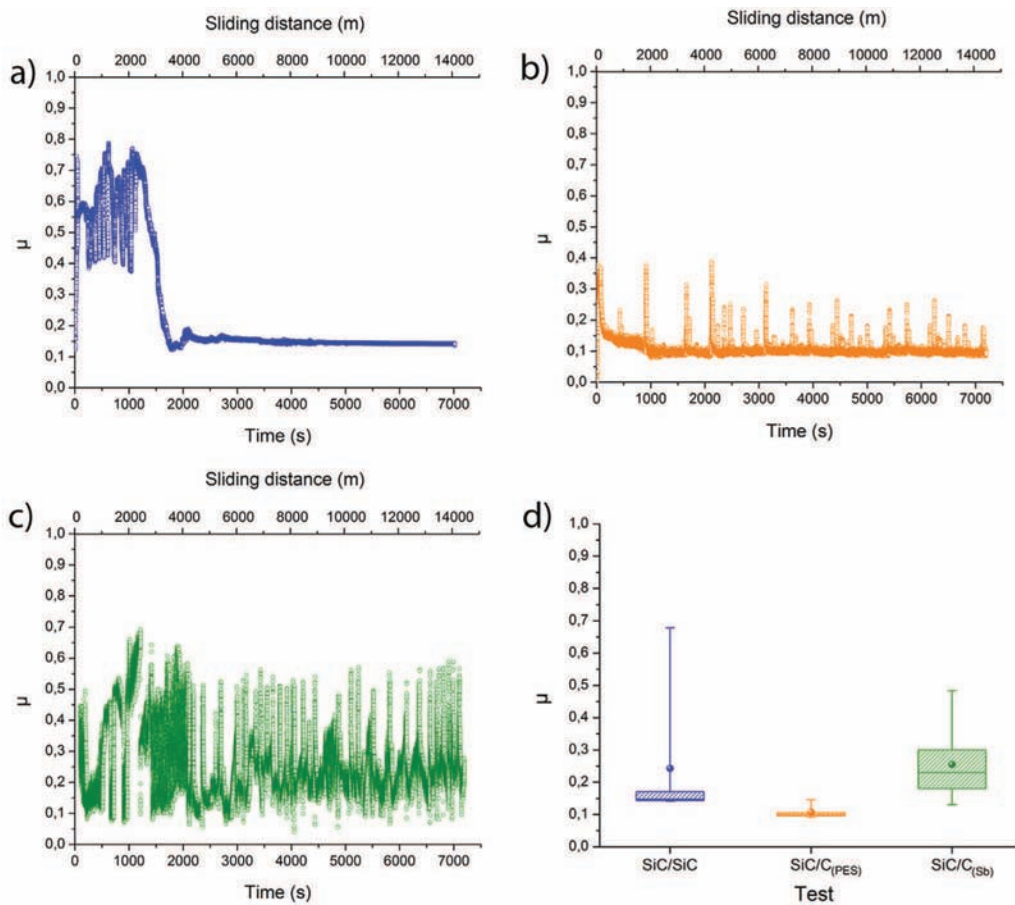


Fig. 3. Friction coefficients: SiC/SiC (a), SiC/C_(PES) (b), SiC/C_(Sb) (c) and distribution (d).

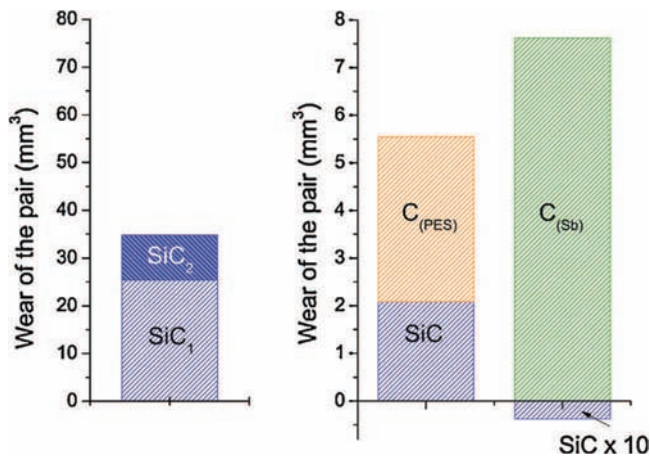


Fig. 4. Wear volumes of the tested pairs.

3.2. Wear volumes

Fig. 4 shows the wear volume of ring specimens for each test. The SiC/SiC pair exhibited a high mass loss, with a difference of one order of magnitude with the pairs using carbon materials. Using carbon samples as counter-faces decreased the wear volume of the couple and particularly of SiC. Moreover, while there was a transfer of material on the SiC surface for the pair using C_(Sb), there was a shared wear for the pair with C_(PES). The high hardness of silicon carbide did not prevent its wear and only the use of C_(Sb) had a protective effect on it.

3.3. Worn surfaces observations and analyses

3.3.1. Optical microscopy

Micrographs of the worn counter-face surfaces (upper rings) are shown in Fig. 5. A tribofilm appeared on both silicon carbide and carbon surfaces. This tribofilm, deposited in the sliding direction, creates a separation between the surfaces and accommodates the speed between the rotating silicon carbide and the fixed counter-face.

Debris were deposited onto the inner area of the SiC (white grey) while they were more spread out onto the carbon samples. At a macro scale, the two carbon surfaces C_(PES) and C_(Sb) seem quite similar, showing the tribofilm formed by the debris deposited on the whole friction area.

3.3.2. SEM microscopy

Fig. 6–8 show SEM images of the same surfaces at a smaller scale, where differences between the samples are revealed. The tribofilm found on the SiC sample after a SiC/SiC test (Fig. 6) shows a powdery plates shape inhomogeneously spread over the surfaces with some cracks due to a cooling effect that happened after the friction test.

Scratches from abrasion are observed in the sliding direction on the C_(PES) surface (Fig. 7) and large debris are also trapped inside depressions created by the material extraction on the wear track.

The debris found on the C_(Sb) surface (Fig. 8) are smaller and a thick tribofilm was formed. The surface of the C_(Sb) does not

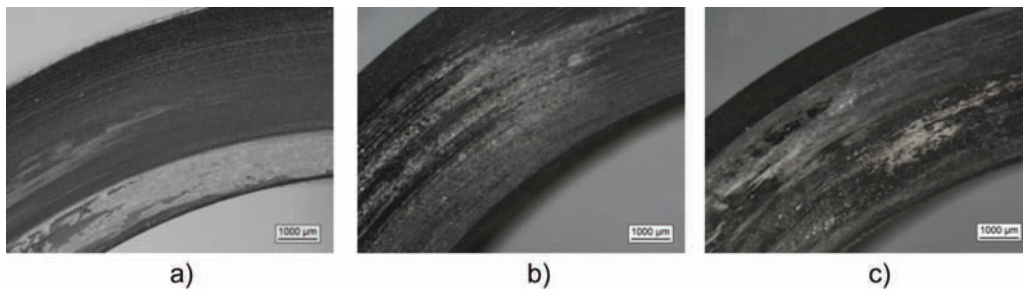


Fig. 5. Micrographs of the worn surfaces: from SiC/SiC friction test (a), C_(PES) (b) and C_(Sb) (c).

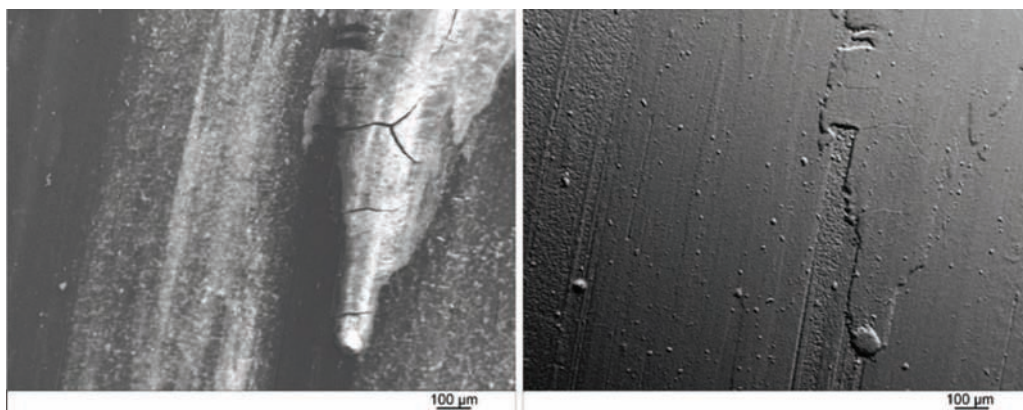


Fig. 6. SEM images of the worn surfaces (left: secondary electron beam, right: backscattered electron beam): SiC (a) from SiC/SiC friction test.

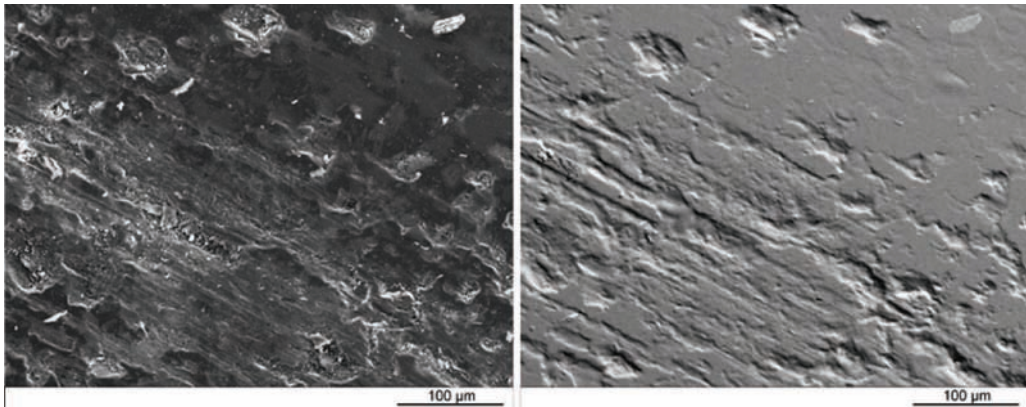


Fig. 7. SEM images of the worn surfaces (left: secondary electron beam, right: backscattered electron beam): SiC (a) from SiC/C_(PES) friction test.

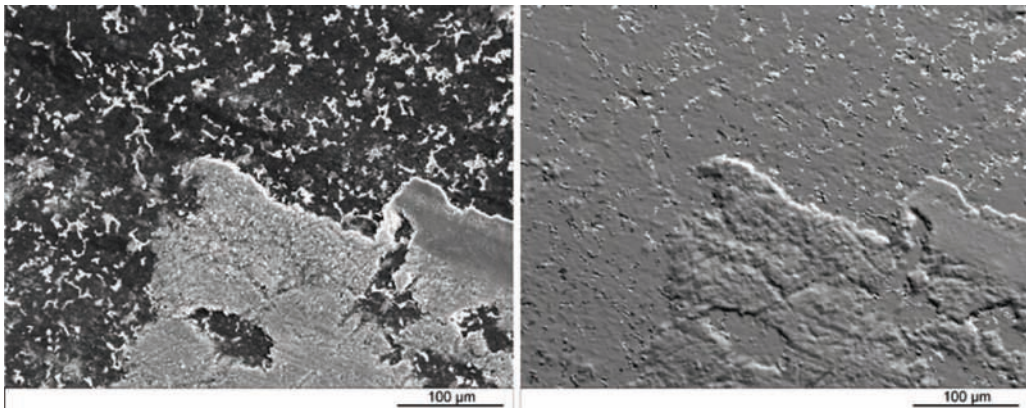


Fig. 8. SEM images of the worn surfaces (left: secondary electron beam, right: backscattered electron beam): SiC (a) from SiC/C_(Sb) friction test.

show any scratch or big removal of material and is fairly close to the initial surface compared to the C_(PES). This initial surface can be seen in Fig. 8, on the left: black regions are identified as carbon and white regions as antimony. As a summary of the morphology and topography analysis of the worn surfaces, it seems that each couple involved different wear mechanism and

that the impregnation also played a role on the formation of the tribofilm.

Using EDS, the chemical composition of the tribofilms is found to be mainly composed of carbon and oxygen. Looking at the oxygen maps (Figs. 9 and 10), the tribofilm is observed and covers the initial samples.

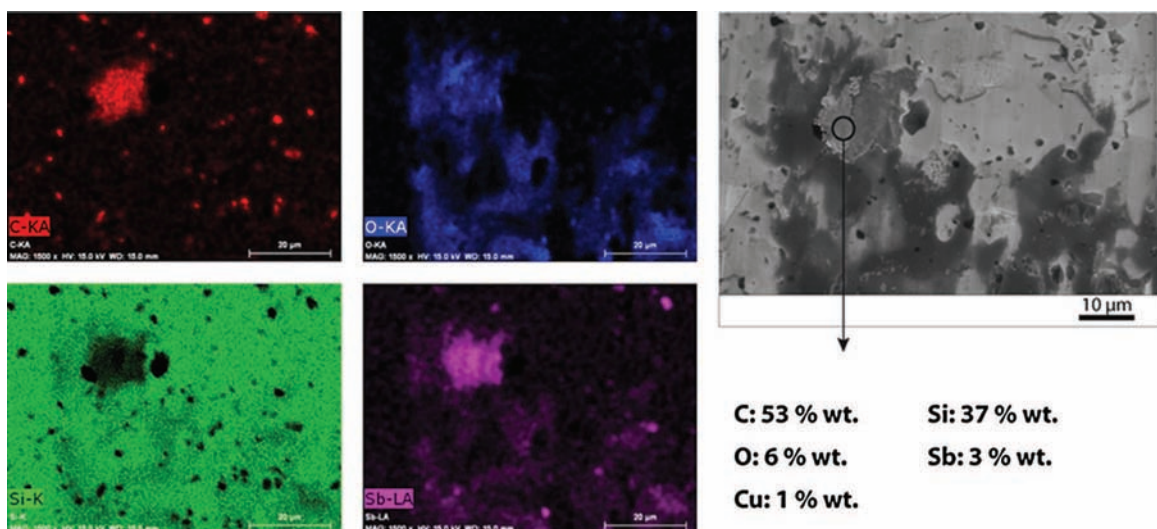


Fig. 9. SEM image and EDS analysis of worn SiC surface from SiC/C_(Sb) friction test.

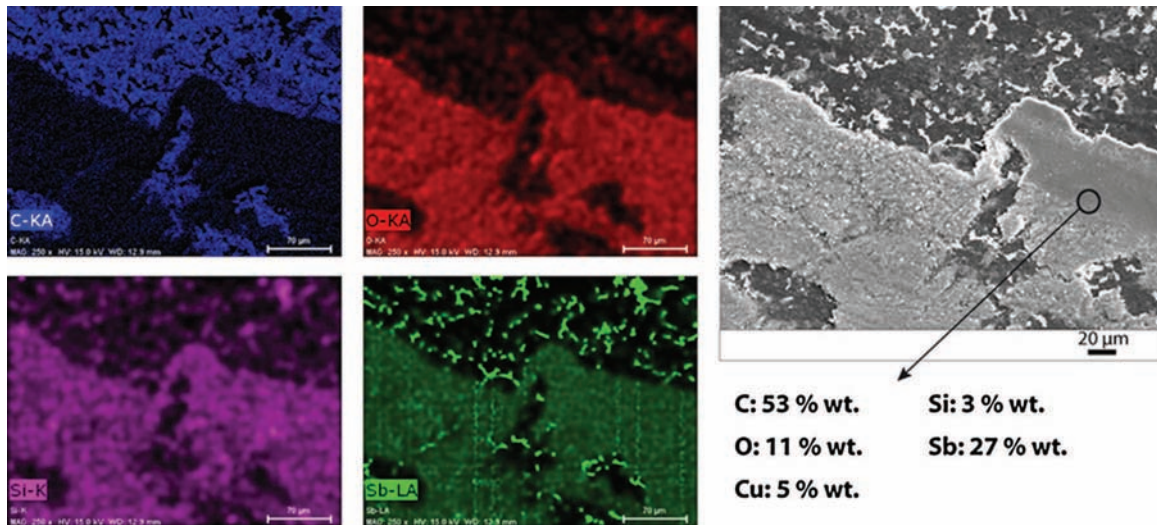


Fig. 10. SEM image and EDS analysis of $C_{(Sb)}$ surface.

In the case of the $SiC/C_{(Sb)}$ test, the impregnant is seen within this tribofilm, following oxygen traces. An oxide of antimony mixed with carbon makes up the tribofilm at the interface of the two sliding specimens. In addition, a small amount of silicon on the surfaces of carbon materials was also revealed (Fig. 10) testifying the wear of the SiC sample.

In summary, the tribofilms created at the interface are composed by the elements of the initial specimens and undergo an oxidation process which leads to the set-up of material flow at the interface.

3.3.3. Raman spectroscopy

As shown by the scheme given by Colomban,¹⁴ the Raman spectroscopy assesses the molecular species signature by the peaks position on the Raman spectrum, the crystallinity of the molecules and finally, the mechanical stresses by the shift of peaks position on the spectrum (Fig. 11).

A chemical analysis was realized on the samples before and after friction: silicon carbide, carbon graphite and antimony were followed. A focus is made on the crystallinity of graphite at the sliding interface and graphite crystallite size was measured.

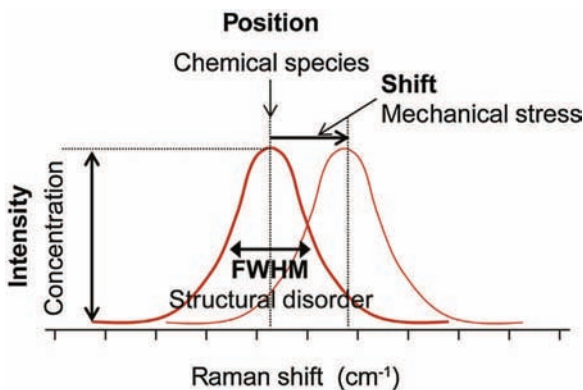


Fig. 11. Contribution of the Raman spectroscopy.¹⁴

Finally, the evolution with friction of the mechanical stresses on the samples is assessed.

Chemical analysis The SiC spectrum (Fig. 12) can be divided in two regions. Between 100 and 700 cm^{-1} , the peaks related to the folded longitudinal and transversal acoustic modes (FLA and FTA) are observed. The peaks related to the folded longitudinal and transversal optical modes (FLO and FTO) are seen between 700 and 1000 cm^{-1} .

In this study, the focus is on the most intense FLO and FTO modes. The presence of three polytypes was identified at the initial state: SiC -4H, -6H and -15R; written in the Ramsdell notation.¹⁵ These polytypes differ by their crystalline lattice and stacking order. The associated Raman spectrum is a combination of these polytypes from which some peaks are characteristics of one polytype. For example, the peak at 789 cm^{-1} characterizes the SiC -6H, the peak at 777 cm^{-1} , the SiC -4H and the peak at 785 cm^{-1} , the SiC -15R (Table 2). Regarding the evolution of the silicon carbide structure with friction process, neither the nature of these polytypes, nor their population, nor the full width at

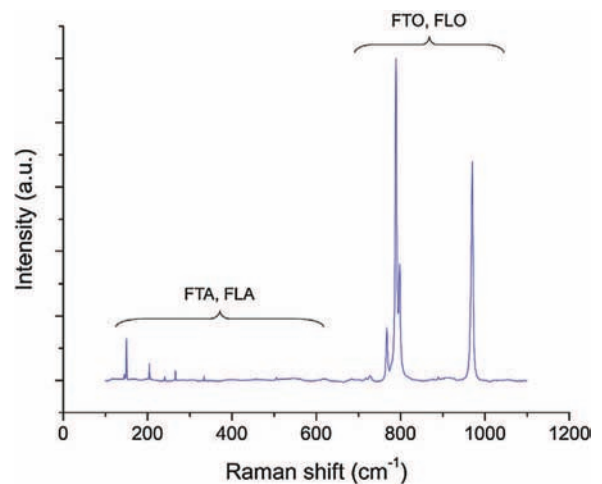


Fig. 12. SiC BOOSTEC[®] Raman spectrum.

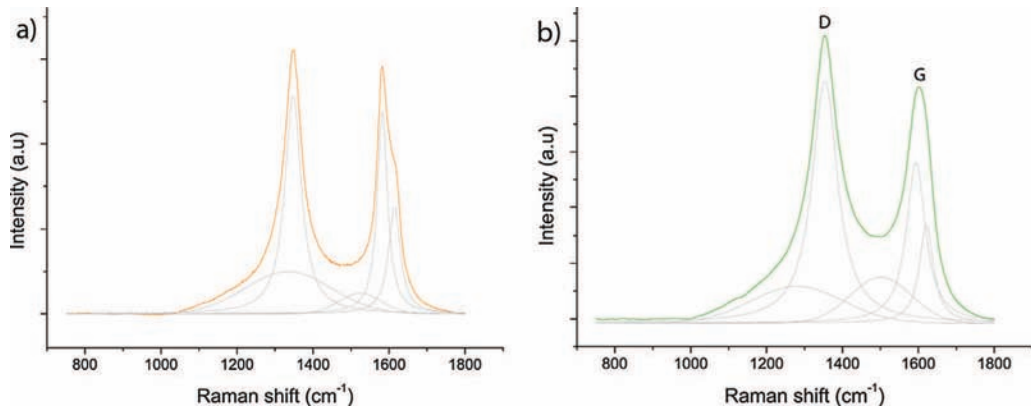


Fig. 13. Raman spectra of $C_{(PES)}$ (a) and $C_{(Sb)}$ (b) at initial state with their fitting.

Table 2
Raman peaks of SiC BOOSTEC® (the modes in bold refers to common modes.)

Polytype	Mode	Symmetry	Raman shift (cm^{-1})
6H	FTA	E_2	145
		E_2	150
	FLA	E_1	235
		E_1	241
		A_1	505
		A_1	514
	FTO	E_2	767
		E_2	789
		E_1	798
	FLO	A_1	889
A_1		970	
4H	FTA	E_2	197
		E_2	204
	FLA	E_1	266
		A_1	614
		E_2	777
	FTO	E_1	798
		A_1	970
15R	FLA	A_1	334
	FTO	E_1	798
	FLO	A_1	970

half maximum of the highest peak at 789 cm^{-1} , were changed. The structure of the silicon carbide samples was not impacted by friction.

The Raman spectra of the two carbon-graphite $C_{(PES)}$ and $C_{(Sb)}$ show two peaks, one peak around $1580\text{--}1600\text{ cm}^{-1}$ related to monocrystalline graphite, which is called G and a second peak around 1350 cm^{-1} , called D (Fig. 13, Table 3).

Another peak called D' , related also to disorder, appears on $C_{(PES)}$ spectrum and merges with G for $C_{(Sb)}$. The best fitting of

Table 3
Raman peaks of graphite.

Peak name	Mode symmetry	Raman shift (cm^{-1})
D	A_{1g}	1350
G	E_{2g}	1580
D'	–	1620

the curves was obtained with five peaks: D, G, $D' + 2$ at ~ 1100 and $\sim 1400\text{ cm}^{-1}$ as proposed by Ferrari and Robertson.¹⁶ The origin of these two last peaks is quite uncertain but it is often related to an amorphization process.

For all the friction tests with carbon-graphite samples, the analysis of the silicon carbide Raman spectra reveals now polycrystalline graphite with the G and D bands (Fig. 14). These spectra were first normalized by the height of the SiC-6H peak at 789 cm^{-1} . In SiC/C couples, a transfer phenomenon of particles from the C ring to the SiC ring is confirmed.

Furthermore, for the SiC/SiC test, the presence of polycrystalline graphite on the top surface means that the clusters of graphite that were observed at the initial state in the SiC microstructure (Fig. 1) take part into the friction process.

In the case of the $C_{(Sb)}$, the antimony is also detected by Raman spectroscopy (Fig. 15). As reported in the literature, the ratio A_{1g}/E_g is close to 3¹⁷ but the peaks are shifted downwards when compared to references^{18–20} (Table 4). A downward shift of the A_{1g} and E_g modes is generally detected under compression and below 8 GPa; where a transition of the ambient phase of antimony, showing a rhombohedral structure, is observed. In this range of pressure, the linear pressure coefficients -3.5 and $-3.8\text{ cm}^{-1}/\text{GPa}$ are described for the A_{1g} and E_g modes,

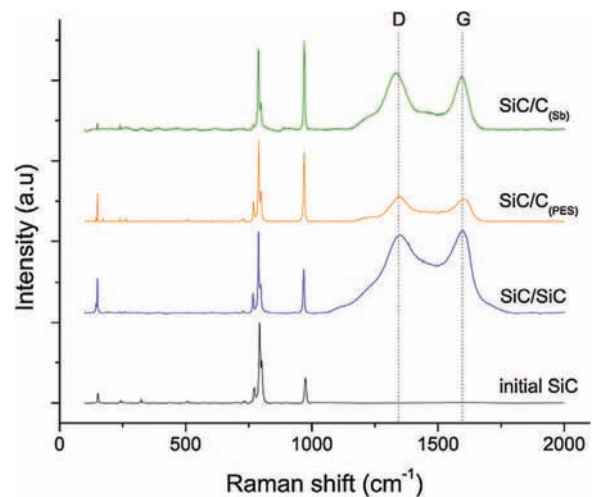


Fig. 14. Raman spectra of worn silicon carbide surfaces.

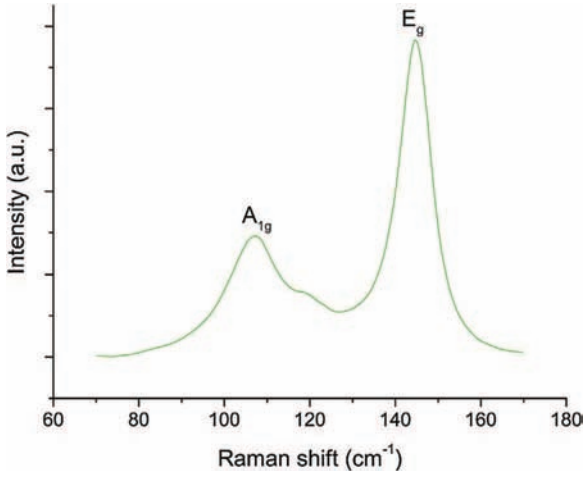


Fig. 15. Antimony Raman spectrum from $C_{(Sb)}$.

Table 4
Raman peaks of antimony.

Mode symmetry	Raman shift (cm^{-1})	References Raman shift (cm^{-1}) ¹⁸⁻²⁰
E_g	106	110–115
A_{1g}	144	149–151

respectively.²⁰ Here, it suggests that the Sb phase sustains a compressive stress about 1.9 GPa.

The material transfers observed with EDS were confirmed with Raman spectroscopy. The presence of the impregnant, particularly in the case of SiC/ $C_{(Sb)}$ test, is revealed in the tribofilm. Following the trace of the antimony, the oxidation process of the tribofilm is also shown by the presence of a new compound: the antimony trioxide, in the senarmonite phase, which is the cubic phase of Sb_2O_3 ²¹ (Table 5). Fig. 16 shows its Raman spectrum that was recorded on the silicon carbide sample after a SiC/ $C_{(Sb)}$ test. This outcome gives an idea of the maximum temperature that was reached during friction as this compound is stable below 570 °C.²² Moreover, the A_{1g} mode of Sb phase is still observed after friction, therefore antimony was only partially oxidized.

Table 5

Raman peaks of Sb_2O_3 (senarmonite phase) - * the peak does not refer to the spectrum of Sb_2O_3 but to initial Sb.

Mode symmetry	Raman shift (cm^{-1})	References Raman shift (cm^{-1}) ²¹
B_2	–	82
E	118	118
A_{1g}	151*	–
B_2	189	189
A_1	254	254
E	–	355
B_2	373	373
A_1	451	450
B_2	–	712

A pressure release happened during friction on the antimony cluster as the position of the A_{1g} peak is closer to 151 cm^{-1} .

Graphite crystallite size. The peak D (Fig. 13) is known to be the result of disorder inside the polycrystalline graphite due to a particle size effect.²³ Its intensity is inversely proportional to the crystallite size L_a for $\lambda = 514.5$ nm through the so-called Tuinstra and Koenig's equation:

$$L_a(\text{nm}) = 4.4 \times R^{-1}, \text{ with } R = \frac{I_D}{I_G} \quad (2)$$

More recently, Ferrari and Robertson¹⁶ demonstrated the non-validity of the Tuinstra and Koenig model for crystallite length lower than 2 nm and proposed a new model for $\lambda = 514.5$ nm and this range of L_a :

$$L_a(\text{nm}) = 1.35 \times R^{1/2} \quad (3)$$

The crystallographic structure of the tribofilm was assessed by making Raman spectroscopy maps of the surfaces ($50 \mu\text{m} \times 50 \mu\text{m}$) before and after each test (Fig. 17). Points of the map are separated by a step of $3 \mu\text{m}$ and each of them linked to one Raman spectrum. At the end, 266 spectra for each sample were processed. The ratio of the intensities of the D and G peaks I_D/I_G was first plotted. As shown previously, this ratio is linked to the crystallites length L_a through Eq. (2). Additionally, the full width at half maximum of the G peak $FWHM_G$ and the area of the amorphous peak at $\sim 1400 \text{ cm}^{-1}$ were monitored.

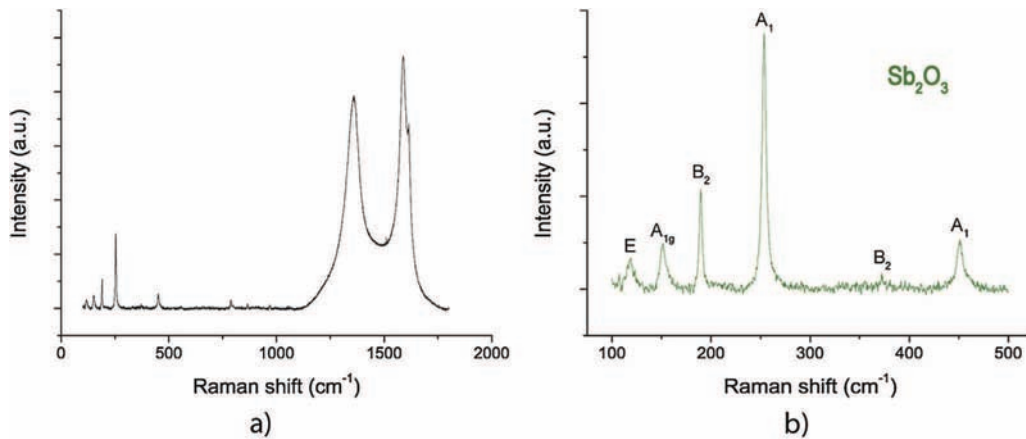


Fig. 16. Raman spectrum of the tribofilm after a SiC/ $C_{(Sb)}$ test (a) and the presence of antimony trioxide is well identified in the range of 100–500 cm^{-1} (b).

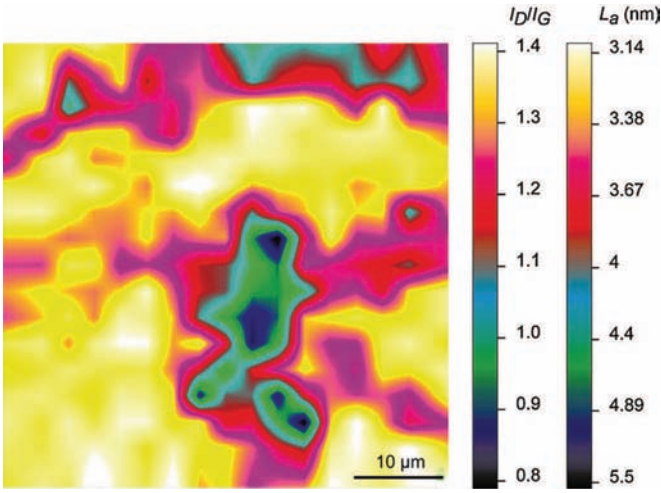


Fig. 17. Raman map of the I_D/I_G ratio for $C_{(PES)}$.

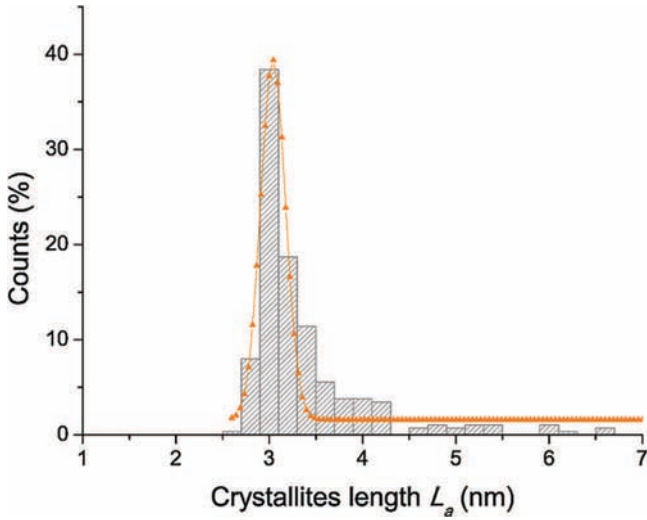


Fig. 18. Gaussian fitting of the distribution of L_a represented on bar diagrams.

The results on the L_a values are first represented on bar diagrams where the distribution of the crystallites length is plotted before and after friction, here for the initial $C_{(PES)}$ (Fig. 18). Then, a Gaussian curve is adjusted to fit the distribution. Table 6

Table 6
FWHM_G and Mean L_a before and after friction for $C_{(PES)}$ and $C_{(Sb)}$.

Material	$C_{(PES)}$	$C_{(Sb)}$
FWHM_G (cm⁻¹)		
Before friction	53.5	58.5
After friction	69.1	83.2
Mean L_a (nm)		
Before friction	3.4	2.8
After friction	4.2	4.1

shows the FWHM_G of the G peak and the mean crystallite length values.

The FWHM_G increased with friction. Therefore, friction induced disorder and thus, amorphization on the top surface of the material. This result is also highlighted by the intensification of the amorphous peak (~ 1400 cm⁻¹) area, as it can be seen in Fig. 19.

However, an increase of the mean L_a is also shown on Fig. 20 and could be attributed to a graphitization process during friction which does contradict the previous result. Furthermore, as viewed previously, the temperature did not exceed 570 °C and was not high enough to cause graphitization. Nonetheless, graphitization is reached after a long time at a very high temperature over 3000 °C. To conclude, it seems that friction removes the short crystallites from the surfaces in favour of the largest ones that cause the increase of the mean L_a .

Mechanical stresses. Mechanical stresses σ are linked to the shift of peak position through the Liu and Vohra's equation (4) for silicon carbide,²⁴ centred on the highest peak of SiC-6H and the Schindler and Vohra's equation (2) for carbon samples,²⁵ centred on G peak. σ is given in GPa in Eqs. (4) and (2).

$$\text{SiC} : \bar{\nu}_{TO}(\text{cm}^{-1}) = 789.2 + 3.11\sigma - 0.009\sigma^2 \quad (4)$$

$$\text{C} : \bar{\nu}_{(E_{2g})}(\text{cm}^{-1}) = 1580 + 4.32\sigma - 0.0408\sigma^2 \quad (5)$$

Raman maps of the peaks position of SiC-6H at 789 cm⁻¹ and of G peak for carbon samples were made (Fig. 21).

The results are first represented on bar diagrams where the distribution of mechanical stresses is plotted, here for $C_{(PES)}$ before friction (Fig. 22) with the Gaussian fitting.

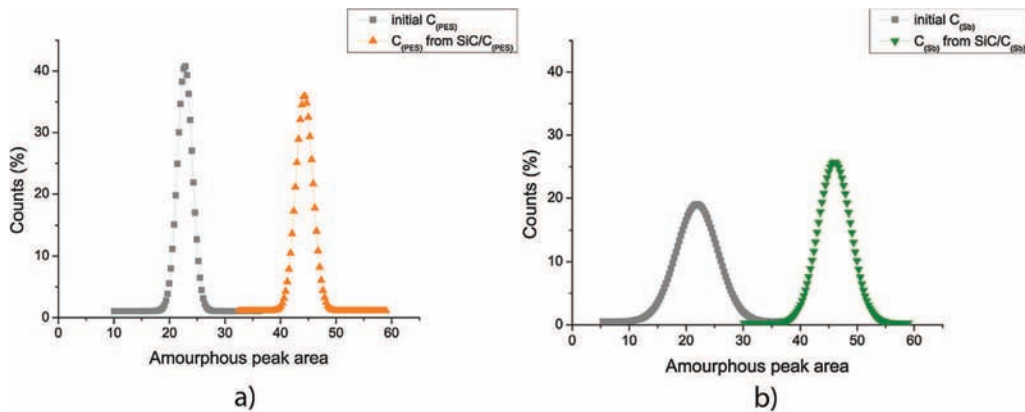


Fig. 19. Distribution of the area of the amorphous peak at ~ 1400 cm⁻¹: $C_{(PES)}$ before and after friction (a), $C_{(Sb)}$ before and after friction (b).

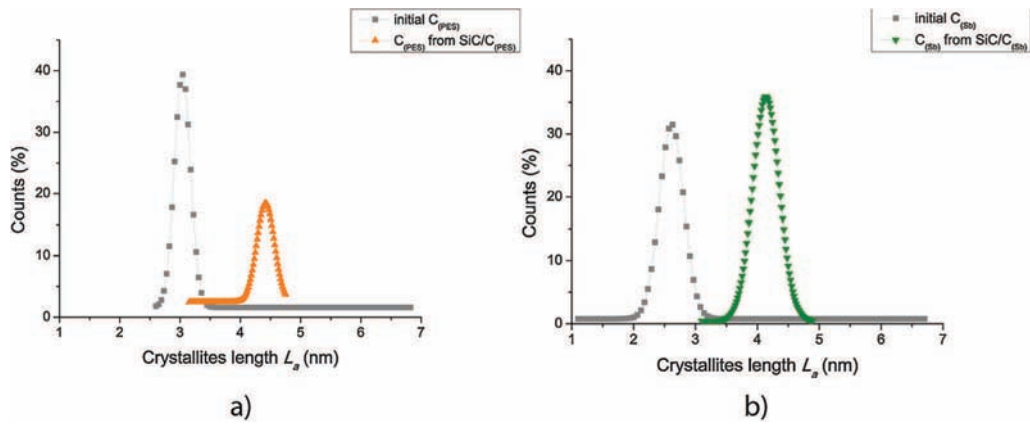


Fig. 20. Distribution of the crystallites length L_g : $C_{(PES)}$ before and after friction (a), $C_{(Sb)}$ before and after friction (b).

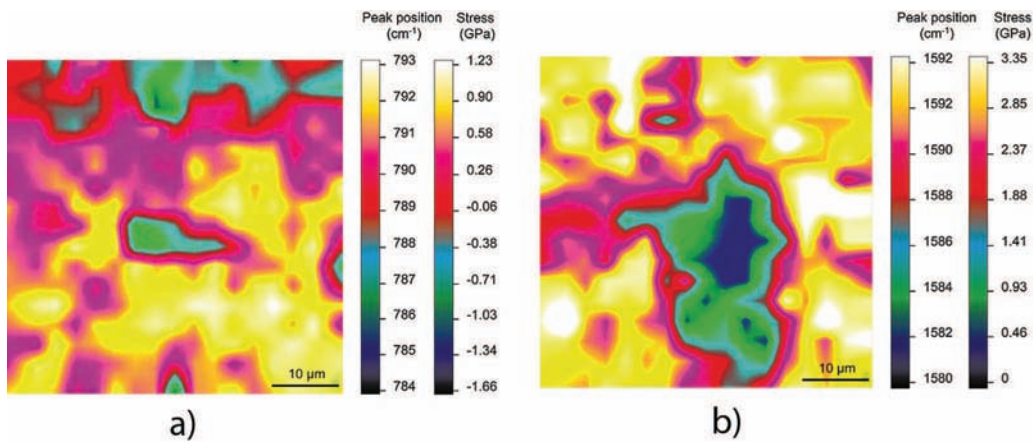


Fig. 21. Raman maps of the mechanical stresses before friction: SiC (a) and $C_{(PES)}$ (b).

All the Gaussian curves for SiC, $C_{(PES)}$ and $C_{(Sb)}$ before and after friction are presented on Fig. 23. Table 7 shows the mean mechanical stresses σ and Table 8 the full width at half maximum ($FWHM_\sigma$) of the mechanical stress distribution.

The initial stress field on SiC is mainly compressive (Fig. 23a) with a mean value of 0.5 GPa. After friction it decreases to -0.18 ± 0.43 GPa, -0.42 ± 0.33 GPa, 0.29 ± 0.45 GPa after friction against SiC, $C_{(PES)}$ and $C_{(Sb)}$, respectively.

Table 7

Mean σ before and after friction for all the friction tests.

Material		Mean σ (GPa)	
		Before friction	After friction
SiC/SiC	SiC	0.46 ± 0.51	-0.18 ± 0.43
	SiC	0.46 ± 0.51	-0.42 ± 0.33
SiC/ $C_{(PES)}$	$C_{(PES)}$	2.47 ± 0.84	3.47 ± 0.57
	SiC	0.46 ± 0.51	0.29 ± 0.45
SiC/ $C_{(Sb)}$	$C_{(Sb)}$	3.40 ± 1.17	4.33 ± 0.55

Table 8

$FWHM_\sigma$ before and after friction for all the friction tests.

Material		$FWHM_\sigma$ (GPa)	
		Before friction	After friction
SiC/SiC	SiC	0.77	0.81
	SiC	0.77	0.51
SiC/ $C_{(PES)}$	$C_{(PES)}$	0.87	0.46
	SiC	0.77	0.99
SiC/ $C_{(Sb)}$	$C_{(Sb)}$	2.65	0.84

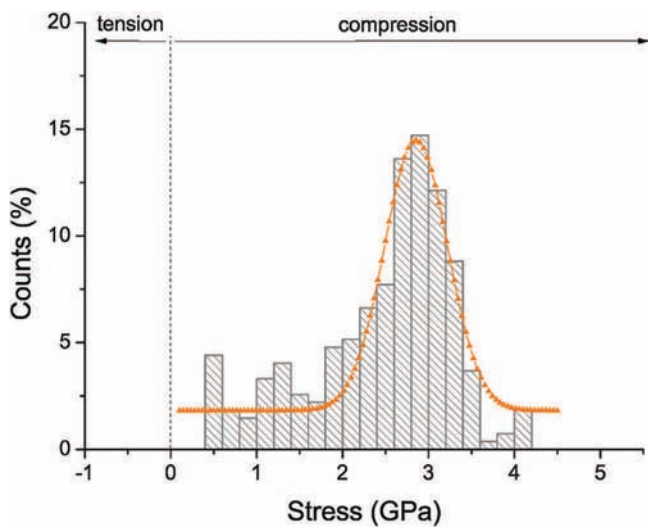


Fig. 22. Gaussian distribution of the mechanical stresses for $C_{(PES)}$ at initial state.

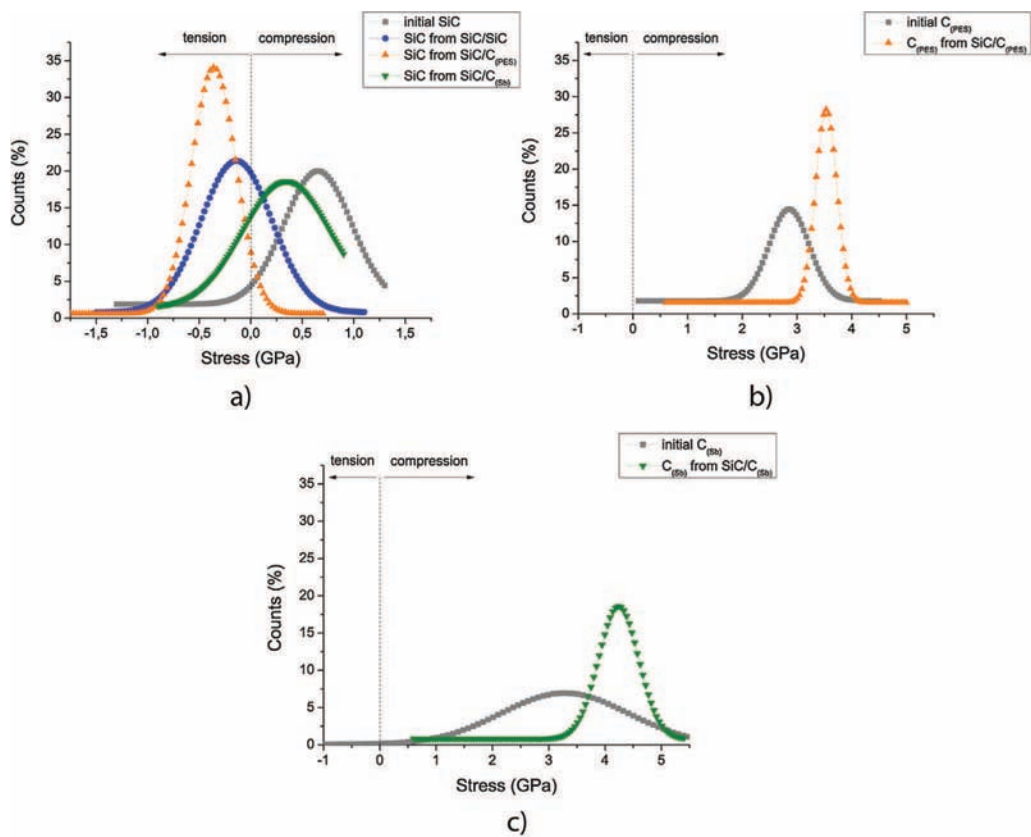


Fig. 23. Distribution of the mechanical stresses: SiC (a), C_(PES) (b) and C_(Sb) (c).

Generally, on brittle material such as SiC, this stress field could proceed from a change in the microstructure or a cracking process inside the material. However, as previously concluded, the SiC structure was not impacted by friction. Therefore, the main possible damaging mode of silicon carbide was cracking. Friction against C_(Sb) induced the lowest stress field on SiC which is in good accordance with the result obtained for the wear measurements. In the case of the two carbon materials C_(PES) and C_(Sb), the initial stress field increase is tightly compressive. After friction, the carbons increase their compression level (Fig. 23b and c) of 40% and 27%, respectively. The difference of mechanical stresses distribution at initial states between the two materials is removed by friction. Regarding the full width at half maximum of the mechanical stresses distribution $FWHM_{\sigma}$, it seems that friction tends to homogenize the stress at the surface of the materials. For both carbons, the material was in overpressure and damaged quickly, leading to a high wear.

4. Discussion

The three different couples of this study reveal three different behaviours. This seems to be related to the nature of the impregnation material in the carbon ring. In agreement with our observations, we propose three mechanisms of degradation for the following couples: SiC/SiC - SiC/C_(PES) and SiC/C_(Sb).

In the first case (Fig. 24), both SiC surfaces produce a source flow of matter (Q_{s1} , Q_{s2}). The production of particles is due to a fracture phenomenon that has been identified by measurement

of residual tensile stresses at their surface. These fractures cause detachment of clusters of SiC from the surface.

When two SiC rings slide one against the other, the interface is filled not only with SiC particles but also grains of pyrographite and B₄C. The pyrographite acts as a lubricant, and B₄C, in agreement with its high hardness plays the same role as SiC and contributes to the abrasive wear. Porosities are considered as sites of accumulation of debris and also places where fracture phenomena could be preferentially initiated. This third body circulates in the contact and constitute the internal flow (Q_i).

Molecules from the atmosphere (Q_{ext}), in peculiar O₂ and H₂O, can be introduced into the contact and can contribute

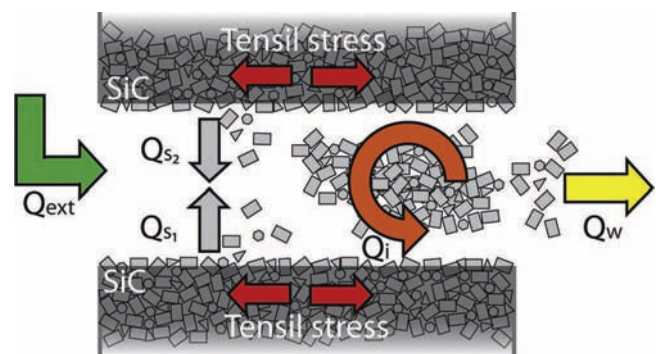


Fig. 24. Wear mechanism proposed for a SiC/SiC couple. Red arrows represent the tensile stress at the surface of the 2 first bodies. (For interpretation of the references to color in this text, the reader is referred to the web version of the article.)

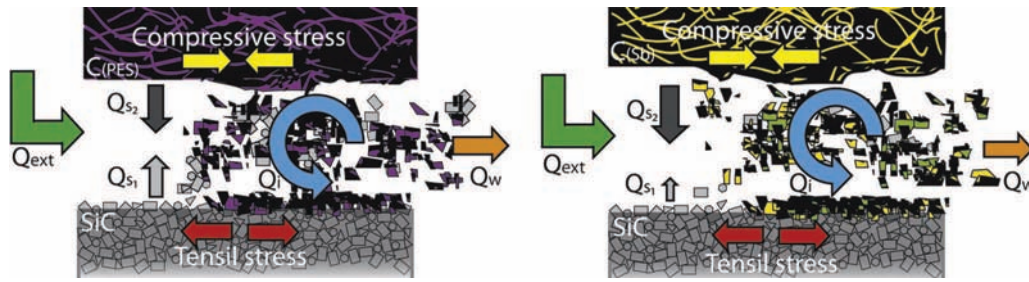


Fig. 25. Wear Mechanism for a SiC/C_(PES) couple (a) and a SiC/C_(Sb) couple (b).

significantly in this process. After a transition period, the third body circulates between the two rings (Q_i). The friction coefficient is low because of this layer of debris and the regime is stable.

But this film of particles is abrasive and accentuates wear. Fractions of the third body are ejected with an external flow (Q_w) and both rings lose continuously matter throughout the end of the test.

With the SiC/C_(PES) couple (Fig. 25a), the SiC ring behaviour is similar to the SiC/SiC initial degradation mechanism and SiC particles are fractured from the surface. However, the quantities emitted are 10 times smaller (Q_{s1}). The presence of the carbon-graphite ring, as a counter-face, reduces the intensity of the surface stress. However, the mechanical stress is mostly supported by the C_(PES) ring and due to compression, particles are broken and milled from the carbon-graphite surface (Q_{s2}). This mechanism causes the amorphization of graphite grains but the particles with a size around 4 nm remain stable in the internal flow (Q_i). Mixed with the SiC particles, they constitute the third body.

Finally, in the last case, with the SiC/C_(Sb) couple, the C_(Sb) ring emits a lot of particles because of compressive stresses (Q_{s2}). The amorphous carbon and also graphite particles of 4 nm size are maintained in the interface. EDX and Raman spectroscopies permit us to reveal that antimony react with oxygen from the external flow (Q_{ext}) and antimony (III) oxide is produced by the reaction (6):



In this last case, the surface stresses do not initiate the flow of SiC particles and the film is largely made of graphite particles, amorphous carbon, antimony and its oxide (Fig. 25b). This third body avoids the transmission of mechanical stress to the SiC ring (Q_i). Moreover, a fraction of tribofilm adheres to the SiC surface and constitutes a screen. This third body seems to be adhesive, thus, sometimes both rings are stuck together and this conducts to an unstable stick-slip regime during the sliding motion.

This SiC/C_(Sb) couple, is the most efficient in terms of protection of the SiC surface even though the stability of the sliding regime is not improved. The C_(Sb) ring loses a lot of matter (Q_w). Its wear resistance has to be enhanced.

Unlike the SiC/C_(Sb) couple, the SiC/C_(PES) couple does not prevent wear of the SiC surface. However, this couple is the

most efficient of this study by reducing the stick-slip regime and giving the smallest friction coefficient of the three.

5. Conclusions

SiC/SiC and SiC/C couples for mechanical seal applications were tested under sliding friction at 120 °C. SiC/C couples presented two grades of carbon-graphite: one, impregnated by polyester resin and, another one, by antimony. These pairs of materials present different tribological behaviors in terms of friction coefficient and wear. Using characterization methods such as electronic microscopy and Raman spectroscopy allowed building a relevant wear mechanism for the tested tribopairs. Mechanical stresses, crystallinity of the tribofilm and material transfer were assessed.

In the case of a SiC/SiC couple, we highlighted that the tensile stresses on the surface of the rings lead to the propagation of cracks on the surface and the flow of abrasive debris (SiC, B₄C) and lubricating pyrographite particles into the interface. Mechanical seals made with silicon carbide operating in dry sliding conditions led to unfavourable wear.

The replacement of the SiC counter-face by carbon-graphite reduces by one order of magnitude the wear loss of the pair by first protecting the silicon carbide samples, particularly with the C_(Sb) ring. But the mechanisms involved are different according to the impregnated compound.

The carbon ring emits particles in the interface due to compressive stresses. Those particles are crushed in fine grains, a fraction can be amorphized and constitute the third body. Moreover, another fraction of particles is ejected out of the interface.

- When the ring is impregnated with antimony a tribo-activated phenomenon of oxidation appears in surplus and causes the formation of Sb₂O₃, well identified by Raman spectroscopy. In this situation, the high adhesion of the tribofilm created by the antimony impregnated carbon lead to a high stick-slip phenomenon.
- This is not the case of the tribofilm produced with an impregnation with polyester resin that tends to strengthen mechanical ring and reduces mechanical stress. The use of the polyester resin impregnant reduces the friction coefficient level but also, the frequency of creation-destruction of the tribofilm and thus, improves its stability. In addition, the polyester resin gives

greater wear resistance of the carbon–graphite by restraining the compressive mechanical stresses increase.

This study showed that the ability for the carbon materials to create a stable third body inside the contact controls the performances of the couple.

Acknowledgements

Financial support received from ANRT and CG65 is gratefully acknowledged. The authors would like to thank Mr. Olivier Marsan, CIRIMAT-ENSIACET (Toulouse), for his assistance on the Raman spectroscopy.

References

1. Zum Gahr KH, Blattner R, Hwang DH, Pohlmann K. Micro- and macro-tribological properties of SiC ceramics in sliding contact. *Wear* 2001;**250**(12):299–310, 13th International Conference on Wear of Materials.
2. Murthy VSR, Kobayashi H, Tamari N, Tsurekawa S, Watanabe T, Kato K. Effect of doping elements on the friction and wear properties of SiC in unlubricated sliding condition. *Wear* 2004;**257**(1-2):89–96.
3. Bartelt G. Sliding friction and wear of ceramic/ceramic couples lubricated with hexadecane. *Tribol Ser* 1995;**30**:635–58. Lubricants and Lubrication, Proceedings of the 21st Leeds-Lyon Symposium on Tribology.
4. Amutha Rani D, Yoshizawa Y, Hyuga H, Hirao K, Yamauchi Y. Tribological behavior of ceramic materials (Si₃N₄, SiC and Al₂O₃) in aqueous medium. *J Eur Ceram Soc* 2004;**24**(11):3279–84.
5. Cranmer DC. Friction and wear properties of monolithic silicon-based ceramics. *J Mater Sci* 1985;**20**:2029–37.
6. Denape J, Lamou J. Sliding friction of ceramics: mechanical action of the wear debris. *J Mater Sci* 1990;**25**:3592–604.
7. Fundus M, Knoch H. Diamond like carbon coatings-tribological possibilities and limitations in applications on sintered silicon carbide bearings and seal faces. In: *14th International Pump Users symposium*. 1997. p. 93.
8. Khurshudov AG, Olsson M, Kato K. Tribology of unlubricated sliding contact of ceramic materials and amorphous carbon. *Wear* 1997;**205**(1-2):101–11.
9. Zaidi H, Paulmier D, Jeanmaire A, Nery H. Behaviour of graphite in friction under various environments: connection with the surface reactivity. *Surf Sci* 1991;**251-252**:778–81.
10. Stempfplé P, von Stebut J. Nano-mechanical behaviour of the 3rd body generated in dry friction-Feedback effect of the 3rd body and influence of the surrounding environment on the tribology of graphite. *Wear* 2006;**260**(6):601–14.
11. Déprez P, Hivart P, Coutouly JF, Debarre E. Friction and wear studies using taguchi method: application to the characterization of carbon-silicon carbide tribological couples of automotive water pump seals. *Adv Mater Sci Eng* 2009;**2009**:10. Article ID 830476.
12. Salabura JC, Adamou A, Denape J, Paris JY, Andrieu E. Conception d'un tribomètre environnemental pour l'étude de la réactivité des surfaces frottantes. *Mec Ind* 2006;**7**:311–6.
13. Adamou AS, Denape J, Paris JY, Andrieu E. Mise au point d'un tribomètre environnemental: application l'étude d'un alliage base nickel. In: Presses Universitaires Romandes, editor. *Tribologie et conception mécanique, JIFT 2004*. 2006. p. 95–106.
14. Colomban P. Imagerie Raman de matériaux et dispositifs hétérogènes. In: *Techniques de l'ingénieur, no. RE5*; 2002. p. 311–6.
15. Lefevre J. *Etude des effets d'irradiation dans le polytype cubique du carbure de silicium par les techniques spectroscopiques de photoluminescence et de résonance paramagnétique électronique [Ph.D. thesis]*. France: Ecole Polytechnique, Université à Palaiseau; 2008.
16. Ferrari A, Robertson J. Interpretation of Raman spectra of disordered and amorphous carbon. *Phys Rev B* 2000;**61**:14095–107.
17. Lannin JS, Calleja JM, Cardona M. Second-order Raman scattering in the group-V_b semimetals: Bi, Sb and As. *Phys Rev B* 1975;**12**:585–93.
18. Degtyareva O, Struzhkin VV, Hemley RJ. High-pressure Raman spectroscopy of antimony: as-type, incommensurate host–guest and bcc phases. *Solid State Commun* 2007;**141**:164–7.
19. Wang X, Kunc K, Loa I, Schwarz U, Syassen K. Effect of pressure on the Raman modes of antimony. *Phys Rev B* 2006;**74**:134305.
20. Olijnyk H, Nakano S, Takemura K. Effect of pressure on the Raman modes of antimony. *Phys Status Solidi B* 2007;**244**(10):3572–82.
21. Mestl G, Ruiz P, Delmon B, Knozinger H. Sb₂O₃/Sb₂O₄ in reducing/oxidizing environments: an in situ Raman spectroscopy study. *J Phys Chem* 1994;**98**(44):11276–82.
22. Freedman LD, Doak GO, Long GG, Mahmood T, Lindhal CB. Antimony compounds. In: *Kirk-Othmer Encyclopedia of Chemical Technology*. Wiley-Interscience; 2007. p. 2762. Fifth edition.
23. Tuinstra F, Koenig JL. Raman spectrum of graphite. *J Chem Phys* 1970;**53**(3):1126–30.
24. Liu J, Vohra YK. Raman modes of 6H polytype of silicon carbide to ultra-high pressures: a comparison with silicon and diamond. *Phys Rev Lett* 1994;**72**(26):4105–8.
25. Schindler TL, Vohra YK. A micro-Raman investigation of high-pressure quenched graphite. *J Phys-Condens Mat* 1995;**7**(47):L637.